

CARDIAC MOTION ANALYSIS USING WAVELET PROJECTIONS FROM TAGGED MR SEQUENCES

Y. Farouj^{1*}, L. Wang^{1‡}, P. Clarysse^{1‡}, L. Navarro², M. Clausel^{3†}, P. Delachartre^{1‡}

¹University of Lyon; CREATIS; CNRS UMR 5220; Inserm U1044, Villeurbanne, France

²École Nationale Supérieure des Mines; CIS-EMSE; CNRS UMR 5307; LGF, F-42023 Saint-Etienne, France

³ University of Grenoble-Alpes; Laboratoire Jean Kuntzmann; CNRS UMR 5224, Grenoble, France

ABSTRACT

We present an optical flow technique in a differential projected framework adapted to local myocardial motion estimation from MR Tagged images. The algorithm is based on the Dual Tree design of Hilbert transform pairs of wavelet bases. Such a design allows one to construct several orientation-sensitive wavelet filters for better analysis of the complex motion of the heart. The complex wavelet transform (CWT) integrates both energy and phase information in the wavelets coefficients for an effective motion estimation. The CWT also provides a high frequency analysis and enjoys a multiresolution aspect that allows multiscale flow estimate. Performances of the algorithm are evaluated on synthetic tagged MRI sequences for both displacement and strain estimation.

Index Terms— Cardiac motion, Tagged MRI, Optical flow, Complex wavelets

1. INTRODUCTION

Tagged Magnetic Resonance Imaging (MRI) provides an effective modality to track the motion of cardiac moving tissues. The concept of this method is to mark tissues with magnetically saturated parallel lines. Tagged MRI generates a dark grid which is deformed with the underlying tissue. Thus, tracking the grid helps the estimation of displacements.

Accurate and robust methods for motion extraction from medical image sequences are essential for the quantification and analysis of the contraction of muscles in the cardiac walls. In computer vision, numerous methods have been proposed along different approaches, exploiting either intensity or energy and phase information. Differential techniques are based on spatiotemporal intensity derivatives assuming that pixel intensity does not change by small displacements. Velocity

is given as the solution of the Optical Flow (OF) constraint equation :

$$\frac{d}{dt}I(t; \mathbf{x}) = \partial_t I + \mathbf{v} \cdot \nabla_{\mathbf{x}} I = 0, \quad (1)$$

where $I(t; x_1, x_2) : \mathbb{R}^3 \rightarrow \mathbb{R}$ is the image sequence, $\partial_t, \nabla_{\mathbf{x}}$ are temporal and spatial derivatives respectively while $\mathbf{v} : \mathbb{R}^3 \rightarrow \mathbb{R}^2$ is the unknown 2D velocity vector. This equation suffers from the *aperture problem* as there is two unknowns. To overcome this issue Horn and Schunck [1] introduced a spatial smoothness constraint. Lucas and Kanade [2] assumed that the flow is constant in a spatial neighborhood. Both methods were tested on MR images in [3] and shown to be sensitive to image quality. Phase-difference methods [4][5] define displacement from the shift necessary to align phase outputs values from spatiotemporal filtered input images. Accuracy of such methods depends on the temporal support of filters increasing computational complexity. This latter approach imposes an additional assumption on the time dependence of the optical flow which might not hold in cardiac motion because of the discontinuity of the velocity field at the end of the isovolumic relaxation for example. Methods using only two frames were developed using the phase of the analytic signal and have shown to be accurate in ultrasound imaging [6], when the brightness invariance does not necessarily hold because of the through plane movement of the heart.

In this work, we exploit a multi-channel strategy initiated by Weber and Malik [7]. It consists in filtering images by spatial filters and applying equation (1) to each channel. The over-constrained system is directly solved by a least square technique with performances comparable to phase based-methods. Bernard [8] used a particular spatial filtering using wavelet transform. Compared to the classical projection of Weber and Malik, the wavelet projection provides a natural multiscale framework and an important computational gain due to the fast wavelet transform. For our application the use of complex wavelet transform is motivated by the fact that such a filtering gives access to the high frequency information present in tags. Instead of the analytic wavelet transform used by Bernard, we use the Dual Tree Complex Wavelet

*This work was supported by "Région Rhône-Alpes" under the ARC 6.

†M. Clausel's research was supported by the French Agence Nationale de la Recherche (ANR) under reference ANR-13-BS03-0002-01 (ASTRES).

‡Authors within the framework of the Labex CELYA ANR-10-LABX-0060 and Labex PRIMES ANR-11-LABX-0063 of Université de Lyon, within the program "Investissements d'Avenir" ANR-10-LABX-0060/ANR-11-IDEX-0007 operated by the ANR.

Transform, which provides six orientation sensitive wavelets to accurately capture heart motion in several directions. In addition, scaling coefficients from the wavelet transform are taken into account. This provides low frequency analysis to help countering noise effects.

2. REAL AND COMPLEX WAVELET TRANSFORM

We denote by ψ and ϕ respectively the *scaling function* and the *wavelet function* in the 1-D discrete wavelet transform (DWT). The standard 2-D DWT consists of the tensor products of 1-D DWTs over each dimension : the scaling function $\phi(x_1)\phi(x_2)$ represent low frequencies and three subband wavelets $\psi(x_1)\psi(x_2)$, $\phi(x_1)\psi(x_2)$, and $\psi(x_1)\phi(x_2)$ oriented in the diagonal, horizontal, and vertical directions, respectively. This transform is equivalent to bandpass filtering with a subsampling step to remove redundancy.

The DWT suffers from major drawbacks. Some of them are related to the motion estimation approach that will be presented. First, small shifts of the signal generates important changes on the wavelets coefficients and energy is not conserved. Second, wavelet coefficients tend to oscillate positively and negatively around singularities and so passes often though or close to zero. This fact makes the inversion of matrices of wavelets coefficients particularly unstable. Finally, the lack of directional selectivity due to the separable tensor product construction which produces filters simultaneously oriented along several directions. The Complex Wavelet Transform (CWT) effectively overcomes shift invariance and oscillations [9]. This is due to the fact that the CWT has an analytic representation which is close to the Fourier representation thus shifts are encoded in a simple linear phase offset while the magnitude is an invariant non oscillating envelope (cf. third row in figure 1).

A particular design of the CWT known as the Dual Tree CWT (DT CWT) [10] produces wavelets which are supported only in one quadrant of the 2-D frequency domain. These wavelets are not only analytic but also directional selective, providing six bandpass subimages oriented at $\pm 15^\circ$, $\pm 45^\circ$ and $\pm 75^\circ$ and thus cover more distinct orientations than the separable DWT or other analytic wavelets. The DT CWT employs two real DWTs from two different sets of filters. The two sets of filters are jointly designed so that the overall transform forms a Hilbert pair. We note respectively the *scaling function* and the *wavelet function* $\phi^c = \phi_h + j\phi_g$ and $\psi^c = \psi_h + j\psi_g$. The complex 2-D wavelets are then constructed, for all $\mathbf{x} = (x_1, x_2)$ in $L_2(\mathbb{R}^2)$, as follows :

$$\psi^{1,1}(\mathbf{x}) = \phi^c(x_1)\psi^c(x_2), \quad \psi^{2,1}(\mathbf{x}) = \phi^c(x_1)\overline{\psi^c(x_2)}, \quad (2)$$

$$\psi^{1,2}(\mathbf{x}) = \psi^c(x_1)\psi^c(x_2), \quad \psi^{2,2}(\mathbf{x}) = \psi^c(x_1)\overline{\psi^c(x_2)}, \quad (3)$$

$$\psi^{1,3}(\mathbf{x}) = \psi^c(x_1)\phi^c(x_2), \quad \psi^{2,3}(\mathbf{x}) = \psi^c(x_1)\overline{\phi^c(x_2)}, \quad (4)$$

where \bar{f} represents the complex conjugate of f . Each of the six wavelets is aligned in a specific direction, as shown in

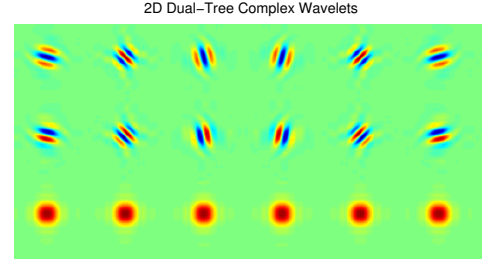


Fig. 1. Impulse response of the filter set generated by the DT CWT at a single scale. From left to right : $\psi^{1,1}$, $\psi^{1,2}$, $\psi^{1,3}$, $\psi^{2,3}$, $\psi^{2,2}$, $\psi^{2,1}$ (cf. equations (2)-(4)). First row : real part, second row : imaginary part and third row : magnitude.

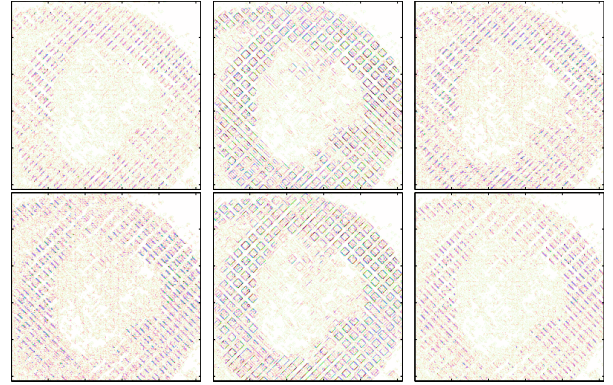


Fig. 2. The real parts of the six wavelets outputs from a tagged MR image of a myocardium (First decomposition level).

figure 1. For the sake of simplicity in the sequel, the resulting scaling functions will be denoted by :

$$\phi^1(\mathbf{x}) = \phi^c(x_1)\phi^c(x_2), \quad \phi^2(\mathbf{x}) = \phi^c(x_1)\overline{\phi^c(x_2)}, \quad (5)$$

As mentioned before, these wavelets have characteristics similar to those of the Fourier transform, thus estimating disparity using the projected version of equation (1) on such a wavelet bases integrate both phase and energy information. Instead of resolving directly the OF equation, we estimate disparity from filtered versions of the input images with high frequency information to get profit from tagging (Figure 2). Note that motion estimation techniques using complex wavelets were initially developed in [11]. Authors used the coefficients phase shifts to estimate local translations.

3. PROJECTED OPTICAL FLOW METHOD

The method described in our work uses the wavelet approach to overcome the aperture problem and estimate the

flow field $\mathbf{v} = (v_1, v_2)$. Let us consider the wavelets basis $(\psi^{i,j})_{(i,j) \in \{1,2,3\}^2}$ and the scaling function $(\phi^k)_{k \in \{1,2\}}$ both centered around the origin, and let us take the inner product of (1) with the translated versions centered around the point \mathbf{u} defined as $\psi_{\mathbf{u}}^{i,j}(\mathbf{x}) = \psi^{i,j}(\mathbf{x} - \mathbf{u})$ and $\phi_{\mathbf{u}}^k(\mathbf{x}) = \phi^k(\mathbf{x} - \mathbf{u})$ respectively. We obtain the following system for all $(i, j) \in \{1, 2, 3\}^2$ and $k \in \{1, 2\}$:

$$\begin{aligned} \langle \partial_t I, \psi_{\mathbf{u}}^{i,j} \rangle + \langle v_1 \cdot \partial_{x_1} I, \psi_{\mathbf{u}}^{i,j} \rangle + \langle v_2 \cdot \partial_{x_2} I, \psi_{\mathbf{u}}^{i,j} \rangle &= 0, \\ \langle \partial_t I, \phi_{\mathbf{u}}^k \rangle + \langle v_1 \cdot \partial_{x_1} I, \phi_{\mathbf{u}}^k \rangle + \langle v_2 \cdot \partial_{x_2} I, \phi_{\mathbf{u}}^k \rangle &= 0, \end{aligned} \quad (6)$$

where $\langle \cdot, \cdot \rangle$ is the standard inner product in $L_2(\mathbb{R}^2)$.

We make the assumption that the flow is constant in the wavelet and scaling functions supports. Then, system (6) becomes :

$$\begin{aligned} \langle \partial_{x_1} I, \psi_{\mathbf{u}}^{i,j} \rangle v_1(\mathbf{u}) + \langle \partial_{x_2} I, \psi_{\mathbf{u}}^{i,j} \rangle v_2(\mathbf{u}) &= -\langle \partial_t I, \psi_{\mathbf{u}}^{i,j} \rangle, \\ \langle \partial_{x_1} I, \phi_{\mathbf{u}}^k \rangle v_1(\mathbf{u}) + \langle \partial_{x_2} I, \phi_{\mathbf{u}}^k \rangle v_2(\mathbf{u}) &= -\langle \partial_t I, \phi_{\mathbf{u}}^k \rangle. \end{aligned} \quad (7)$$

Thus, for each scale in the wavelet decomposition process, we obtain a system of 8 equations. When projecting only on the wavelet basis and under some assumptions on the regularity of the flow, Bernard [8] proved that the solution of the obtained system converges toward the real flow when the wavelets scale converges to zero. This fact encourages us to work at small scales. Temporal sampling might impose an opposite constraint.

Note that systems of equations at different scales provide a natural multiscale framework. At each scale the flow is bounded by the wavelet support and one can use an appropriate coarse to fine refinement scheme to capture large and small displacements. In all cases, the obtained linear system (7) is of the form $A_{\mathbf{u}} \mathbf{v}(\mathbf{u}) = B_{\mathbf{u}}$, where $\mathbf{v}(\mathbf{u}) = (v_1(\mathbf{u}), v_2(\mathbf{u}))$. Let us denote $M_{\mathbf{u}} = (Real(A_{\mathbf{u}}), Imag(A_{\mathbf{u}}))^T$ and $Q_{\mathbf{u}} = (Real(B_{\mathbf{u}}), Imag(B_{\mathbf{u}}))^T$, the flow vector \mathbf{v} can then be estimated for each pixel \mathbf{u} by a least square technique :

$$\mathbf{v}(\mathbf{u}) = (M_{\mathbf{u}}^T M_{\mathbf{u}})^{-1} M_{\mathbf{u}}^T Q_{\mathbf{u}}. \quad (8)$$

In order to ensure sufficient confidence in the flow field estimates, one can test singularities and round off errors in $M_{\mathbf{u}}^T M_{\mathbf{u}}$ inversion by a simple eigenvalue based threshold process. Actually, this is the only tuning parameter required by the algorithm which makes it easy to handle. Moreover, the algorithm relies on easy matrix computations and the fast wavelet transform which makes it particularly fast.

4. METHOD EVALUATION

We tested our algorithm on synthetic cardiac tagged MR images and derive the strain tensor from estimated displacement. This tensor provides deformation maps for an effective analysis of heart motion. In this section, we present our numerical results with some details on the implementation.

4.1. Implementation

We make use of the filters from [12] for the original wavelet¹. These filters benefit from orthogonality and near-symmetry. For the DT CWT, the Q-shift design [13] is used. This design preserves orthogonality on each tree beyond level 1, matching of the two trees and symmetric subsampling.

A comparison will be presented with the PBDBM method described in [14]. This method is based on phase disparity[6] combined with a block-matching technique. It outperforms the SinMod method [15] widely used for tagged cardiac MR image analysis. For the PBDBM algorithm, the parameters were empirically optimized to yield the smallest average error in our experiment. For our algorithm, experiments on our Dataset did not yield singular matrices. Therefore, the eigenvalue threshold was not applied. We were also able to estimate the motion field from the finest level of the multiscale representation.

4.2. Dataset

We assessed our method on two synthetic tagged MRI sequences generated by the ASSESS software [16] for which the true displacement field was known. These sequences are based on an analytic model providing typical contraction, relaxation, rotation and thickening of the heart in 2D short axis slice. For our study, the first sequence (*P0*) aims to present a healthy heart while a localized motion anomaly (pathological heart) is taken into account in the second (*P1*). In accordance with the real case, the motion anomaly takes form of an infarcted area in the heart muscle that does not participate or participates less than the rest of the myocardium in the global contraction movement. This occurs when a portion of the heart does not receive enough blood because of a stenosis or obstruction of one of the coronary arteries that supplies blood to heart.

4.3. Numerical results

Table 1 summarizes numerical performances measured using both Average Angular Error (AAE), Average End Point Error (AEPE) and their standard deviations σ . The study features 34 displacement images from 35 frames covering an entire cardiac cycle. Only pixels of interest -in the myocardium area- were taken into account. The Euler estimation (Figure 3) measures disparity between successive frames while the Lagrangian approach tend to measure disparity between a current frame and the original position at the beginning of the systolic phase.

In general, phase-based methods including PBDBM robustly estimate sub-pixel displacements at the beginning and the end of the systolic stage (cf. Figure 4(a)). Our approach outperforms PBDBM over the rest of the sequence, especially

¹A software providing this wavelets is available on <http://eeweb.poly.edu/iselesni/WaveletSoftware/>

Table 1. Error measurements from Euler estimation.

	AAE $\pm \sigma$ (in degrees)	AEPE $\pm \sigma$ (in pixels)	CPU time (s)
Proposed (<i>P0</i>)	2.82 ± 1.69	0.065 ± 0.044	59
PBDBM (<i>P0</i>)	3.49 ± 2.20	0.082 ± 0.059	109
Proposed (<i>P1</i>)	2.79 ± 1.65	0.064 ± 0.044	58
PBDBM (<i>P1</i>)	3.41 ± 2.06	0.080 ± 0.056	107

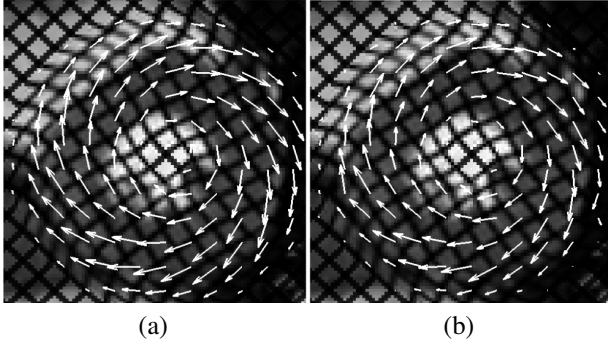


Fig. 3. Euler motion field at the mid-systolic phase (between frames 6 and 7) from sequence *P1*. (a) : True flow, (b) : Our estimation.

when the flow field is of high magnitude. In this latter case it is easier to detect anomalies in the heart motion. Note that the strain tensor is usually displayed from Lagrangian measurements at the end of the systole (frame 15) which corresponds to the maximal displacement in the cardiac cycle. Figure 4(b) shows the accuracy of our estimation at this stage.

Figures 5 and 6 show examples of deformation maps obtained from strain tensors. During the contraction phase, cardiac walls are expected to stretch in the radial direction leading to important deformations. In the pathological *P1* Case, the reduction of the radial strain is clearly visible from our estimation in Figure 6(b).

5. CONCLUSION

We described a new approach for the estimation of heart motion from MR images. A strain analysis was also presented. The results are comparable and better than those of other phase-based methods. The algorithm has low complexity which makes it promising for real-time application for other modalities or for 3D motion estimation. In addition, it enjoys easy handling since no specific parameter tuning is needed. A better directional analysis might be provided by the Monogenic Wavelet Transform (MWT) [17]. However, these wavelets have infinite supports thus the approach we presented does not directly hold. The construction of an appropriate MWTs will be the subject of future works.

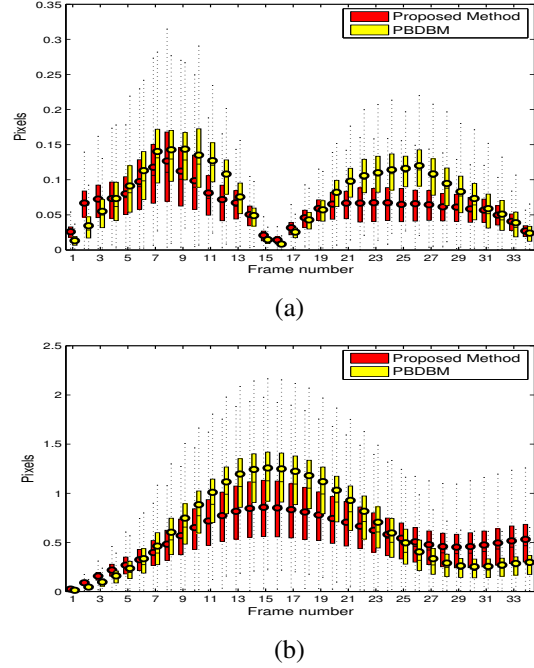


Fig. 4. Boxplot and whiskers of the End Point Errors for sequence *P1*. The center of each box represents the median, the circle gives the average value while the body extends from the 25-th to the 75-th percentile. (a) : Euler displacements and (b) : Lagrange displacements.

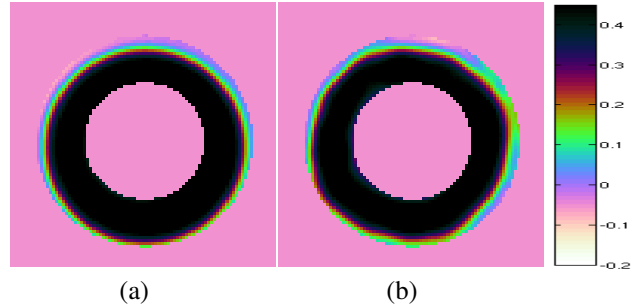


Fig. 5. Radial strain tensor from sequence *P0*. (a) : Ground truth, (b) : Our estimation.

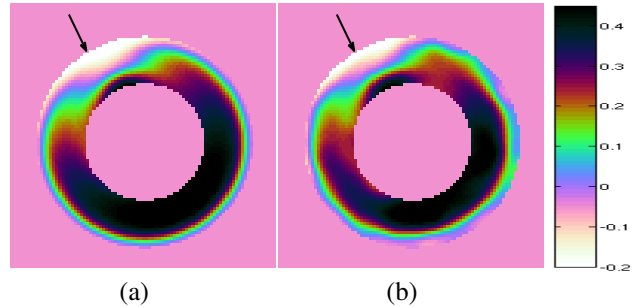


Fig. 6. Radial strain tensor from sequence *P1* with the location of the motion anomaly indicated by the arrow. (a) : Ground truth, (b) : Our estimation.

6. REFERENCES

- [1] B. K. P. Horn and B. G. Schunck, "Determining optical flow," *Artificial Intelligence*, vol. 17, pp. 185–203, 1981.
- [2] B. Lucas and T. Kanade, "An iterative image registration technique with an application to stereo vision," *Proceedings DARPA image understanding workshop*, vol. 130, pp. 121–130, 1981.
- [3] J. L. Barron, "Experience with 3d optical flow on gated mri cardiac datasets," *Proc. CRVO4*, pp. 370–377, 2004.
- [4] D. J. Fleet, A. D. Jepson, and M. R. M. Jenkin, "Phase-based disparity measurement," *CVGIP: Image Understanding*, vol. 53, 1991.
- [5] D. J. Fleet and A. D. Jepson, "Computation of component image velocity from local phase information," *International Journal of Computer Vision*, vol. 5, no. 1, pp. 77–104, 1990.
- [6] A. Basarab, H. Liebgott, and P. Delachartre, "Analytic estimation of subsample spatial shift using the phases of multidimensional analytic signals," *IEEE Transactions on Image Processing*, , no. 2, pp. 440–447, 2009.
- [7] J. Weber and J. Malik, "Robust computation of optical flow in a multi-scale differential framework," *International Journal of Computer Vision*, vol. 14, pp. 12–20, 1994.
- [8] C. P. Bernard, "Discrete wavelet analysis for fast optic flow computation," *Applied and Computational Harmonic Analysis*, vol. 11, no. 1, pp. 32–63, 2001.
- [9] N. G. Kingsbury, "Image processing with complex wavelets," *Phil. Trans. Royal Society London A*, vol. 357, pp. 2543–2560, 1997.
- [10] N. G. Kingsbury, "The dual-tree complex wavelet transform: a new technique for shift invariance and directional filters," in *Proc. 8th IEEE Digital Signal Processing Workshop, Utah*, Aug. 1998, pp. 319–322.
- [11] J. A. F. Magarey and N. G. Kingsbury, "Motion estimation using a complex-valued wavelet transform," *IEEE Trans. on Signal Processing*, vol. 46, no. 4, pp. 1069–1084, 1998.
- [12] A. F. Abdelnour and I. W. Selesnick, "Design of 2-band orthogonal near-symmetric cqf," in *Proc. IEEE Int. Conf. Acoust., Speech, Signal Processing (ICASSP)*, May 2001, pp. 3693–3696.
- [13] N. G. Kingsbury, "A dual-tree complex wavelet transform with improved orthogonality and symmetry properties," in *Proc. IEEE Int. Conf. Image Processing, Vancouver*, 2000, vol. 2, pp. 375–378.
- [14] A. Basarab, P. Clarysse, T. Arts, C. Cachard, P. Croisille, and P. Delachartre, "Estimation de mouvement par décalage de phase et maillage déformable appliquée à des séquences cardiaques d'irm marquées," *Traitement du Signal*, vol. 6, pp. 643–663, 2011.
- [15] T. Arts, F. W. Prinzen, T. Delhaas, J. R. Milles, A. C. Rossi, and P. Clarysse, "Mapping displacement and deformation of the heart with local sine-wave modeling," *IEEE T Med Imaging*, vol. 29, no. 5, pp. 1114–1123, 2010.
- [16] P. Clarysse, J. Tafazzoli, P. Delachartre, and P. Croisille, "Simulation based evaluation of cardiac motion estimation methods in tagged-mr image sequences," *Journal of Cardiovascular Magnetic Resonance*, vol. 13, no. Suppl 1, pp. P360, 2011.
- [17] M. Unser, D. Sage, and D. van de Ville, "Multiresolution monogenic signal analysis using the riesz-laplace wavelet transform," *IEEE Transactions on Image Processing*, vol. 18, no. 11, pp. 2402–2418, November 2009.